Journal of Catalysis 434 (2024) 115532

Contents lists available at ScienceDirect

Journal of Catalysis

journal homepage: www.elsevier.com/locate/jcat

Research article

Cobalt@Ruthenium Core@Shell nanoparticles embedded within nitrogen-doped carbon nanosheets as reversible oxygen electrocatalysts

Shunlian Ning [a,1], Jiayu Lao [e,1], Wei Zhou [c], Yanting Ye [e], Qikai Wu [c], Mingzhe Chen [c], Ming-Hsien Lee [d], Tianchen Cui [f], Dengke Zhao [b,*], Nan Wang [e,*], Shaowei Chen [f,*]

[a] School of Chemistry, Sun Yat-sen University, Guangzhou, Guangdong 510275, China
[b] School of Materials Science and Engineering, Henan Normal University, Xinxiang 453007, China
[c] College of Environment and Energy, School of Environment and Energy, South China University of Technology, Guangzhou Higher Education Mega Center, Guangzhou 510006, China
[d] Department of Physics, Tamkang University, New Taipei 25137, Taiwan
[e] Siyuan Laboratory, Guangzhou Key Laboratory of Vacuum Coating Technologies and New Energy Materials, Department of Physics, Jinan University, Guangzhou, Guangdong 510632, China
[f] Department of Chemistry and Biochemistry, University of California, 1156 High Street, Santa Cruz, CA 95064, United States

ARTICLE INFO

Keywords:
Co@Ru core@shell nanoparticle
Bifunctional oxygen catalyst
Air cathode
Spin state
Rechargeable zinc-air battery

ABSTRACT

Rational design and engineering of cost-effective, high-performance reversible oxygen electrocatalysts for both the oxygen evolution reaction (OER) and oxygen reduction reaction (ORR) is imperative in advancing the progress of rechargeable metal-air batteries (r-MABs). Herein, nanocomposites based on Co@Ru core@shell nanoparticles embedded within N-doped carbon nanosheets (Co@Ru/CS) are prepared via facile galvanic exchange reactions of $RuCl_3$ with Co/NC and used as an effective oxygen electrocatalyst for rechargeable zinc-air battery (r-ZAB). Electrochemical studies demonstrate a remarkable bifunctional catalytic performance of Co@Ru/CS towards both ORR and OER, featuring a low potential gap (ΔE) of only 0.69 V between the OER potential ($E_{10,OER}$) at 10 mA cm^{-2} and half-wave potential ($E_{1/2,ORR}$) of ORR, which is much lower than that of commercial Pt/C + RuO_2 catalysts (0.76 V). Combined studies of experimental characterizations and density functional theory calculations show that the ORR activity arises primarily from the N-doped carbon and CoN_x moieties in the composites, whereas RuO_2/CoOOH produced at high electrode potentials is responsible for the OER activity. Co@Ru/CS based r-ZAB exhibits an open circuit voltage of 1.447 V, specific capacity of 781 mAh g_{Zn}^{-1}, and maximum power density of 115 mW cm^{-2} at 0.83 V, a performance better than that with commercial Pt/C + RuO_2 (1.412 V, 760.56 mAh g_{Zn}^{-1}, and 91 mW cm^{-2}). Results from this research underline the substantial impact of structural engineering on optimizing the electrocatalytic activity of nanocomposites for r-MABs.

1. Introduction

Rechargeable zinc-air battery (r-ZAB) has emerged as a viable energy storage and conversion technology due to the high theoretical energy density (1084 Wh kg^{-1}), minimal environmental impact, and excellent operation safety [1–3]. Nevertheless, the practical use of r-ZAB is hampered by the sluggish electron-transfer kinetics and large polarization overpotentials of the oxygen evolution reaction (OER) during the charge process and oxygen reduction reaction (ORR) during discharge [4]. Currently, Pt-based nanoparticles are the leading catalysts for ORR, whereas ruthenium/iridium oxides (RuO_2/IrO_2) are the catalysts of choice for OER [5]. Yet, these selections are nonideal for r-ZAB as their electrocatalytic activity is limited to a single reaction [6–9]. Therefore, it is imperative to develop viable alternatives that are high-performance, low-cost, and bifunctional.

Within this context, nanocomposites with transition metals encapsulated within N-doped porous carbon (TM@C) have been attracting extensive attention as low-cost bifunctional oxygen electrocatalysts,

* Corresponding authors at: Department of Chemistry and Biochemistry, University of California, 1156 High Street, Santa Cruz, California 95064, United States (S. Chen); School of Materials Science and Engineering, Henan Normal University, Xinxiang 453007, China (D. Zhao); Siyuan Laboratory, Guangzhou Key Laboratory of Vacuum Coating Technologies and New Energy Materials, Department of Physics, Jinan University, Guangzhou, Guangdong 510632, China (N. Wang).
E-mail addresses: scutezhao@sina.com (D. Zhao), nanwang@email.jnu.edu.cn (N. Wang), shaowei@ucsc.edu (S. Chen).
[1] These authors contributed equally to this work.

https://doi.org/10.1016/j.jcat.2024.115532
Received 2 January 2024; Received in revised form 8 April 2024; Accepted 1 May 2024
Available online 3 May 2024

with excellent electrical conductivity, adjustable coordination structure and excellent corrosion resistance [10–15]. Notably, these nanocomposites can even surpass commercial Pt/C towards ORR in alkaline media, but the OER activity has remained largely subpar as compared to commercial RuO_2 and IrO_2 catalysts. This is manifested by a sizeable potential gap ($\Delta E > 0.7$ V) between the OER potential ($E_{10,OER}$) at the current density of 10 mA cm^{-2} and half-wave potential ($E_{1/2,ORR}$) of ORR [16,17]. To render the catalysts active towards both ORR and OER, the OER performance needs to be improved without compromising the ORR activity, and integration of a second material that is OER-active, such as ruthenium compounds [18,19], into TM@C represents an attractive strategy. This calls for a rational design and engineering of the Ru-TM@C nanocomposites.

Herein, nanocomposites based on core@shell-like Co@Ru nanoparticles (NPs) encapsulated within nitrogen-doped porous carbon sheets (Co@Ru/CS) are prepared as efficient bifunctional OER/ORR electrocatalysts via a galvanic exchange reaction using graphitic carbon nitride (g-C_3N_4) as a two-dimensional (2D) thermally removable template. The resulting Co@Ru/CS nanocomposites are found to display a high specific surface area and abundant mesopores, which can facilitate the accessibility of catalytic active sites and electron/mass transfer during electrochemical reactions. As the Ru shells are anchored onto the Co NPs in Co/CS through chemical interactions, the stability of the nanocomposites is markedly enhanced. In electrochemical measurements, Co@Ru/CS displays noble metal-like ORR and OER performances, featuring an $E_{1/2,ORR}$ of + 0.82 V vs. reversible hydrogen electrode (RHE) and $E_{10,OER}$ of + 1.41 V, corresponding to a low ΔE of only 0.69 V. This is markedly better than that of commercial Pt/C + RuO_2 benchmarks ($\Delta E = 0.76$ V). Co@Ru/CS can thus be used as oxygen catalysts for r-ZABs, delivering an open circuit voltage of 1.447 V, specific capacity of 781 mAh g_{Zn}^{-1}, and maximum power density of 115 mW cm^{-2} at 0.83 V, an excellent activity markedly outperforming Pt/C + RuO_2 (1.412 V, 760.56 mAh g_{Zn}^{-1}, and 91 mW cm^{-2}). Combined experimental and computational studies reveal that the ORR activity is due to nitrogen-doped carbon (NC) and CoN_x moieties in Co@CS, while the OER activity mainly arises from RuO_2/CoOOH due to surface reconstruction.

2. Experimental section

2.1. Synthesis of NC and Co/CS

Experimentally, 0.2 g of g-C_3N_4 [20] was added into 200 mL of deionized water under sonication for 15 min. Subsequently, 0.2 mmol of $K_3Co(CN)_6$ was added under stirring for 5 min, followed by the addition of 20 mL of a $Co(NO_3)_2{\cdot}6H_2O$ solution (7.5 mM). Then 0.5 mL of an $NH_3{\cdot}H_2O$ solution was added, followed by 20 mL of a dopamine hydrochloride solution (0.1 g) under stirring for 12 h. After extensive rinsing with deionized water and collection by filtration, the products underwent thermal annealing at 800 °C for 2 h in an argon atmosphere. The resulting sample was labeled as Co/CS. Metal-free NC was prepared in the same manner but without the inclusion of the cobalt salt.

2.2. Synthesis of Ru/CS and Co@Ru/CS

40 mg of Co/CS obtained above was dispersed in 80 mL of deionized water under sonication for 30 min. Subsequently, 150 μL of a $RuCl_3{\cdot}nH_2O$ solution (0.132 mM) was introduced under stirring for 120 min. The resultant dark precipitates were gathered, thoroughly washed multiple times with deionized water, and subjected to drying at 60 ℃, before being thermally annealed at 300 ℃ in an Ar/H_2 atmosphere. The resulting sample was referred to as Co@Ru/CS. Ru/CS was prepared in same way except that NC was utilized in place of Co/CS

2.3. Characterization

Transmission electron microscopy (TEM) measurments were carried out with a Tecnai G2-F20 instrument. Scanning electron microscopy (SEM) images were acquired with a Hitachi S-4800 scope. Wide-angle X-ray diffraction (XRD) patterns were obtained from a Bruker D8-Advance diffractometer. Raman spectra were collected with a HORIBA LabRAM HR Evolution with a 633 nm excitation source or Zolix RTS-mini with a 532 nm continuous laser. Nitrogen sorption measurements were carried out with a Quantachrome Autosorb-iQ-TPX instrument at 77 K.

2.4. Electrochemical measurements

Electrochemical testing was performed in a three-electrode configuration in 1.0 M KOH. Preparation of the catalyst inks involved dispersing 5 mg of the nanocomposites obtained above into 1 mL of a water/isopropanol mixture containing 20 μL of 5 wt% Nafion under sonication for at least 30 min. A calculated amount of the inks were dropcast onto a rotating (gold) ring-(glassy carbon) disk electrode (RRDE) at a mass loading of ca. 0.5 mg cm^{-2}, which served as the working electrode. A graphite rod was used as the counter electrode, while a Ag/AgCl electrode as the reference electrode. The Ag/AgCl electrode was calibrated against a reversible hydrogen electrode (RHE), and all potentials in the present study were referenced to the RHE. The ORR and OER activities were reported by normalizing the current to the geometric area of the RRDE disk electrode.

Linear sweep voltammograms (LSVs) were recorded at the potential scan rate of 5 mV s^{-1}. Electrochemical impedance spectroscopy (EIS) tests were conducted with an AC amplitude of 10 mV within the frequency range of 10,000–0.01 Hz. Electrochemical double layer capacitance (C_{DL}) was estimated by cyclic voltammetry (CV) measurements at non-faradaic potentials. The stability of the catalysts was analyzed by chronoamperometric (i-t) tests at +0.70 V for ORR and +1.45 V for OER.

2.5. Zinc-air battery measurements

A home-made r-ZAB was constructed for battery tests, in which a piece of catalyst-coated carbon paper (at a catalyst loading of 1 mg cm^{-2}) and a polished Zn plate were used as the air cathode and anode, respectively. The electrolyte solution consisted of 6 M KOH and 0.2 M zinc acetate. The constant-current technique was utilized to analyze the cycling stability of the r-ZAB, where a cycle consisted of a discharge step (10 mA cm^{-2} for 6 min), followed by a charge step at the same current density.

2.6. Computational study

Density functional theory (DFT) calculations were carried out using the CASTEP module in Materials Studio. The electronic exchange and correlation effects was described by generalized gradient approximation (GGA) with the Perdew-Burke-Ernzerhof function, and the plane-wave cutoff was tested and set at 500 eV. The self-consistent field tolerance was 2×10^{-6} eV with the ultrasoft pseudo-potential forcore electrons. The Brillouin zone was sampled with a $3 \times 3 \times 1$ Monkhorst-Pack k-point grid. The vacuum space along the z direction was more than 15 Å, which was large enough to avoid interplanar interactions. In order to improve the accuracy and precision of the overall calculation, the Hubbard U correction was applied to Co, and the U value of Co was chosen to be 3.1. The unit cells of CoOOH and RuO_2 were in the R $\bar{3}$ m and P42/mnm symmetry groups, respectively. The hetero-interface model was built by RuO_2 (1 1 0) and CoOOH (0 0 1). All slab models were geometrically optimized and the top layers were allowed to relax.

3. Result and discussion

3.1. Structural characterization

Scheme 1 shows the fabrication procedure of Co@Ru/CS, which entailed two major steps: (a) Co/CS was prepared by thermal annealing using g-C_3N_4 as the thermally removable template, and (b) Co@Ru/CS was synthesized through galvanic reactions involving $RuCl_3$ and metallic Co in Co/CS. TEM measurements were first employed to investigate the structure of the samples. From Fig. S1a, the Co/CS sample can be seen to consist of a number of spherical NPs of 49.3 ± 3.1 nm in diameter distributed onto a sheet-like scaffold. The nanoparticles, as observed in Fig. S1c and d, display distinctive lattice fringes with an interplanar spacing of 0.205 nm that aligns with the *fcc* Co (1 1 1) crystal planes [21]. Selected area electron diffraction (SAED) measurements produced two diffuse rings that can be assigned to Co(1 1 1) and C(0 0 2), respectively (Fig. S1b). These results are consistent with the formation of carbon-encapsulated Co NPs.

A similar morphology can be observed with Co@Ru/CS (Fig. S2), but the average size of the NPs decreased to 17.1 ± 0.8 nm due to $RuCl_3$ etching (Fig. 1**a**), and the Co@Ru/CS sample displays a typical core–shell structure, most likely due to galvanic exchange reactions of Co with Ru(III). In fact, at higher resolutions (Fig. 1**b-c**), clear lattice fringes with a d-spacing of 0.204 nm can be observed with the core, consistent with the *fcc* Co(1 1 1) facets, whereas the shell featured lattice fringes with a d-spacing of 0.234 nm that coincided with the Ru(1 0 0) facets [22,23]. SAED measurements (Fig. 1**c inset**) further confirm the formation of Co and Ru in the sample, where the diffraction rings of Co(1 1 1), Ru(1 0 0) and C(0 0 2) can be readily resolved. The formation of a core–shell nanostructure is also manifested in the line-scan profiles based on energy-dispersive X-ray spectroscopy (EDS), where Ru can be seen to be enriched on the surface of Co nanoparticles (Fig. 1**d**). The corresponding elemental mapping analysis (Fig. 1**e**) reveals that the Co@Ru/CS is composed of C, N, O, Co, and Ru, at a content of 70.4, 2.6, 16.1, 9.7, and 1.2 at.%, respectively (Fig. S3). Notably, the C and O elements were distributed rather evenly across the sample, while Co and Ru show more discrete distributions with a noticeable overlap, again, in good agreement with the formation of Co@Ru NPs embedded within the carbon scaffold.

The specific surface area and corresponding pore-size distribution were then evaluated by nitrogen sorption measurements. Both Co@Ru/CS and Co/CS display a type IV isotherm (Fig. S4a), from which the specific surface area was found to be similar at ca. 449.6 m^2/g for Co@Ru/CS and 454.3 m^2/g for Co/CS, with the pore size mainly within the range of 3 to 10 nm (Fig. S4b), suggesting the predominant formation of mesopores in the samples [24]. XRD measurements of Co@Ru/CS show three characteristic diffraction peaks at 2θ = 44.2°, 51.5°, 75.9° (Fig. 2**a**), in accordance with the Co(1 1 1), Co(2 0 0), and Co(2 2 0) crystalline planes, respectively. Notably, no obvious diffraction patterns of Ru are observed, most likely due to the considerably lower content of Ru in the specimen (Fig. S3). In Raman measurements (Fig. 2**b**), the D and G bands can be identified at 1342 and 1587 cm^{-1} for both Co/CS and Co@Ru/CS, along with a close intensity ratio (I_D/I_G) of 1.02, indicating minimal impacts of Ru incorporation on the carbon substrate.

XPS studies were then conducted to elucidate the electronic structure of the materials. In Fig. 2**c**, the survey spectra for both Co/CS and Co@Ru/CS confirmed the existence of C 1s (284 eV), N 1s (400 eV), O 1s (531 eV) and Co 2p (790 eV) electrons (the latter also possessed an additional peak at 462.5 eV for the Ru 3p electrons). Based on the integrated peak areas, the contents of C, N, O, Co, and Ru in Co@Ru/CS were estimated to be 73.0, 5.8, 11.1, 7.9, and 2.1 at.%, respectively. These values align well with those from the above EDS measurements (Fig. S3). In Fig. 2**d**, the N 1s spectra display four distinct peaks at 398.5 eV for pyridinic N, 399.5 eV for Co-N, 400.8 eV for pyrrolic N, and 401.7 eV for graphitic N (Table S1) [25]. Note that the pyridinic N, Co-N and graphitic N have been known to exhibit good electrocatalytic activity towards ORR [26].

Fig. 2**e** displays the Ru 3p spectrum of Co@Ru/CS, from which two doublets can be deconvoluted. The primary doublet at 461.9/484.0 eV can be attributed to the $3p_{3/2}/3p_{1/2}$ electrons of metallic Ru, while the secondary one at 463.8/485.2 eV to those of Ru^{4+} [27,28]. For the Co 2p spectra (Fig. 2**f**), deconvolution yielded three doublets at 779.1/775.0, 780.7/796.1 and 782.3/797.4 eV for Co/CS, whereas 778.8/774.8, 780.4/795.8 and 782.1/797.2 eV for Co@Ru/CS, in line with the Co^0, Co^{3+} and Co^{2+} $2p_{1/2}/sp_{3/2}$ electrons, respectively [29–31]. It is noteworthy that the peak area corresponding to Co^0 in Co@Ru/CS significantly decreased in comparison to that of Co/CS, consistent with surface etching of Co by $RuCl_3$. Furthermore, it is evident that the Co 2p binding energies of Co@Ru/CS were drastically lower than those of Co/CS, signifying electron transfer from Ru to Co in Co@Ru/CS [32].

3.2. Electrocatalytic activity

Fig. 3**a** shows the ORR polarization curves collected with a RRDE, where Co/CS, Co@Ru/CS, and Pt/C all exhibited a current plateau when the electrode potential was swept negatively, indicative of apparent ORR activity. The onset potential (E_{onset}), which was measured at the current density of 0.1 mA cm^{-2}, was estimated to be +0.945 V for CoCS and +0.914 V for Co@Ru/CS, with the respective $E_{1/2,ORR}$ at +0.837 and +0.832 V, all very close to those of Pt/C (E_{onset} = +0.981 V, $E_{1/2,ORR}$ = +0.840 V). CV measurements yielded similar results, as illustrated in Fig. S5. For Co@Ru/CS prepared with a different $RuCl_3$ feed, the ORR activity varied only slightly with the final Ru content in Co@Ru/CS (Fig. S6). This suggests that the Ru or Co nanoparticles were unlikely the ORR active sites, and the ORR activity most likely arose from the N-doped carbon and CoN_x moieties. The Tafel plots are presented in Fig. 3**b**, where Co/CS exhibits a low Tafel slope of only 48 mV dec^{-1}, in comparison to 58 mV dec^{-1} for Co@Ru/CS and 57 mV dec^{-1} for Pt/C. Fig. 3**c** shows the number of electron transfer involved (n) and the H_2O_2 yield (%), where Co@Ru/CS demonstrate an n value greater than 3.83 within the wide potential range of 0 to +0.8 V, indicative of high selectivity towards the $4e^-$ pathway for ORR, with the corresponding H_2O_2 yield under 3.12 %, which is highly comparable to that of Pt/C (n = 3.90, H_2O_2 yield 3.14 %).

Co@Ru/CS also possessed the highest OER activity among the series (Fig. 3**d**), featuring an overpotential ($\eta_{10,OER}$) of only +180 mV to reach

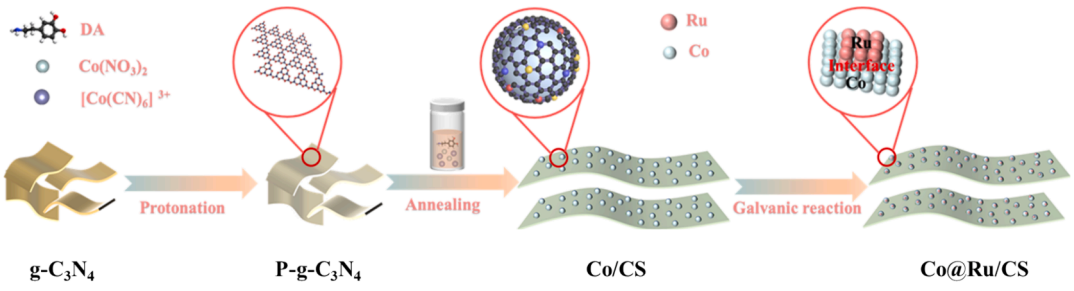

Scheme 1. Schematic illustration of the fabrication process of Co@Ru/CS.

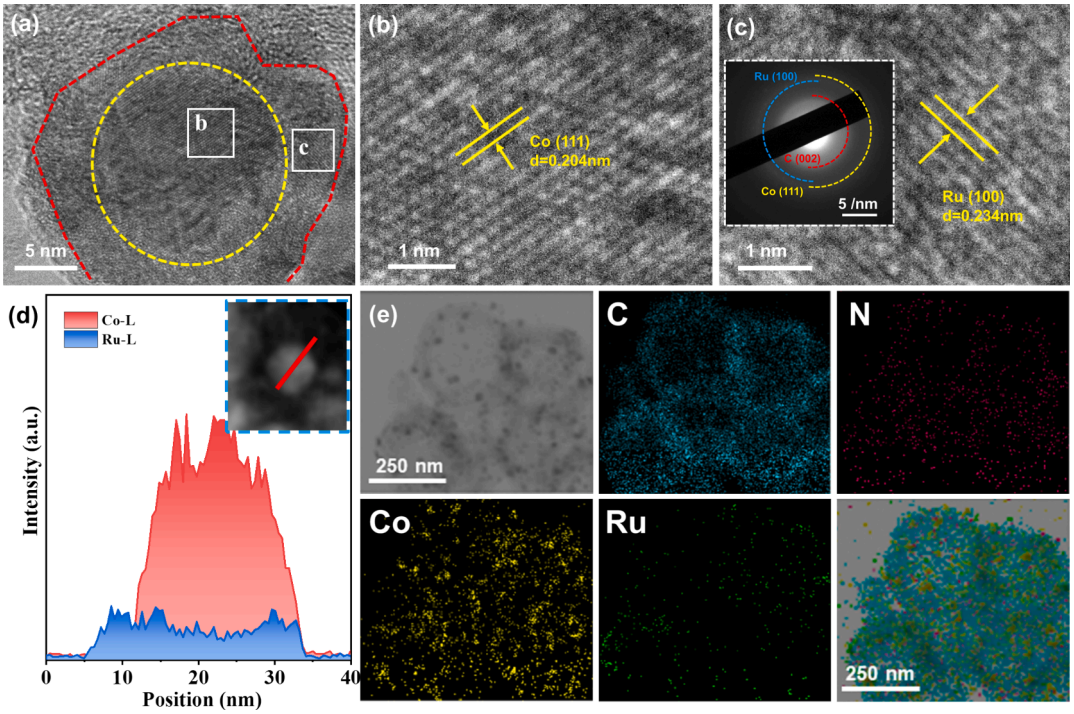

Fig. 1. (a) HRTEM image of Co@Ru/CS. (b, c) Zoom-in images of the boxes in panel (a). Inset to panel (c) is the corresponding SAED patterns. (d) EDS line-scan profiles. Inset is the region of the line scan. (e) EDS-based elemental maps of Co@Ru/CS.

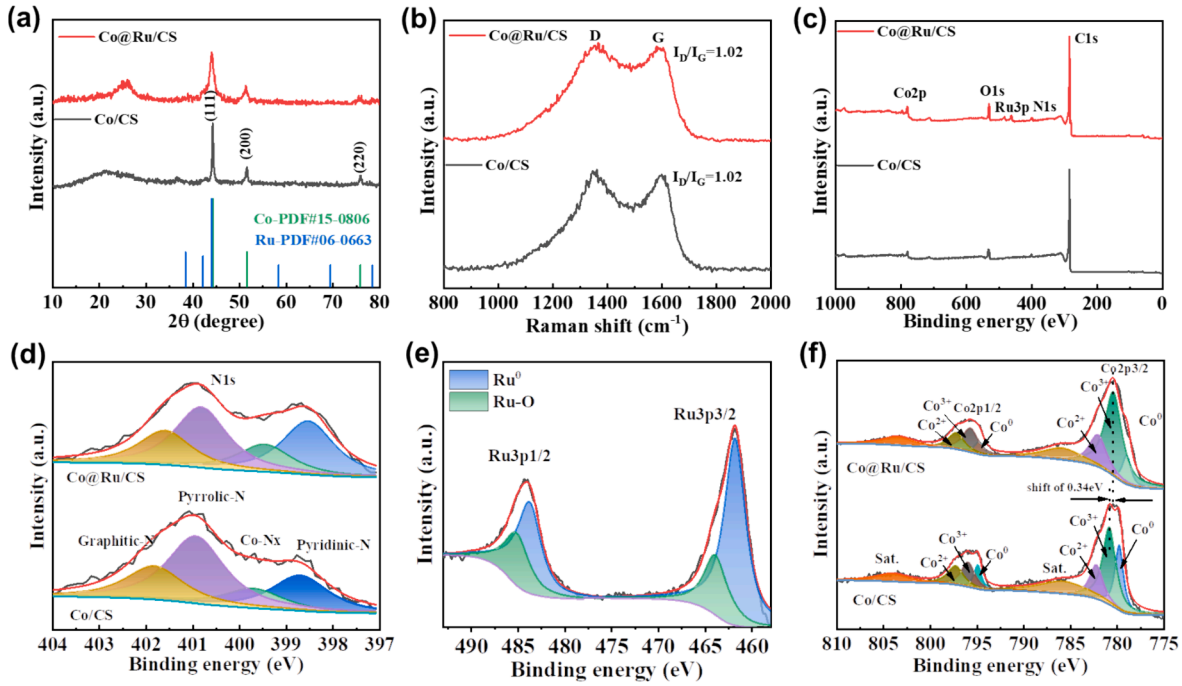

Fig. 2. (a) XRD patterns, (b) Raman spectra, (c) XPS survey spectra, and the corresponding high-resolution scans of the (d) N 1s, (e) Ru 3p and (f) Co 2p electrons of Co/CS and Co@Ru/CS.

the current density of 10 mA cm^{-2}, much lower than that for Co/CS (+310 mV), Ru/NC (over +600 mV), and even commercial RuO_2 (+280 mV). From the Tafel plot in Fig. 3**e,** Co@Ru/CS showed a low Tafel slope of only 58 mV dec^{-1}, much lower than other samples in the series and RuO_2 (67 mV dec^{-1}). In fact, the OER performance of Co@Ru/CS is even better than leading results of relevant Ru-based electrocatalysts documented in the literature **(**Fig. 3**f)** [33–42].

To investigate the influence of Ru on the OER activities, the OER polarization curves of Co@Ru/CS prepared with a different $RuCl_3$ feed were also collected and compared. From Fig. S7, one can find that the OER activity initially rose and then declined with the increase of the $RuCl_3$ feed, indicating that both Ru and Co/CS contributed to the OER activity and the excellent OER performance most likely arose from the synergistic effect of Ru and Co/CS. Fig. 3**g** shows the corresponding

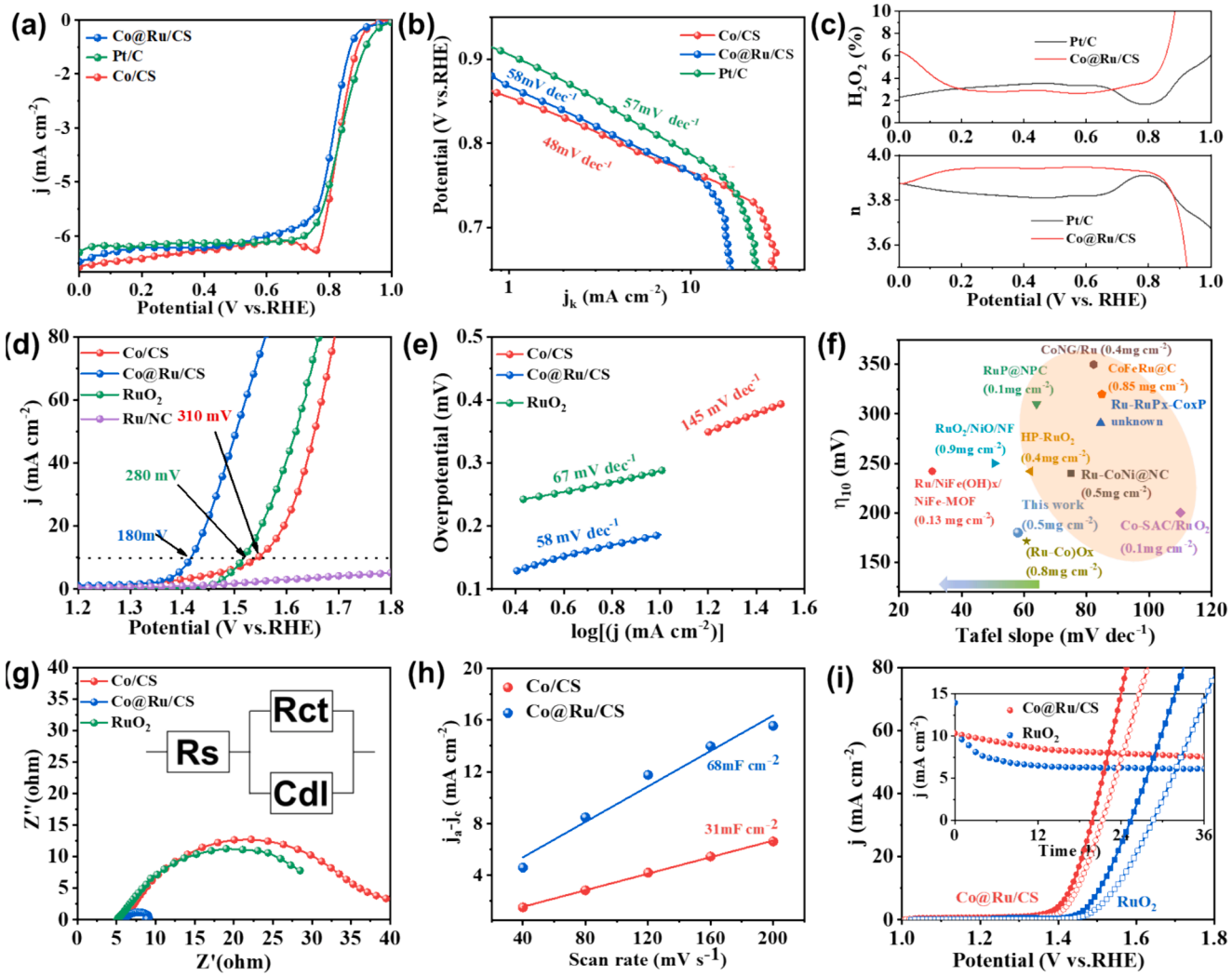

Fig. 3. (a) ORR and (d) OER LSV curves of the sample series, with the corresponding Tafel plots shown in (b) and (e), respectively. (c) n and H_2O_2 yield (%) of the ORR process. (e) OER Tafel plot and (f) $\eta_{10,OER}$ of Co@Ru/CS compared to leading results of relevant electrocatalysts in the literature. (g) Nyquist plots and (h) C_{DL} of the sample series. Inset is the equivalent circuit, where R_S is the serial resistance, R_{CT} is the charge-transfer resistance, and C_{DL} is the double-layer capacitance. (i) OER LSV curves before and after ADT tests. Inset are the i-t curves of RuO_2 and Co@Ru/CS at the applied potential of +0.70 V.

Nyquist plots, where Co@Ru/CS can be seen to exhibit a low charge-transfer resistance (R_{CT}) of only 10 Ω at +1.50 V, compared with 40 Ω for Co/CS and 32 Ω for RuO_2, indicating much enhanced electron-transfer kinetics on Co@Ru/CS. Moreover, the electrode double layer capacitance (C_{DL}) was evaluated by CV measurements in the non-Faradaic potential range (Fig. S8). One can see that Co@Ru/CS possessed a C_{DL} of 68 mF cm^{-1}, drastically greater than that of Co@NC (31 mF cm^{-1}) (Fig. 4**e**), suggestive of improved accessibility of OER active sites in the former.

The ORR and OER stability were then tested by chronoamperometric (i-t) measurements and accelerated decay tests (ADT). Fig. S9a shows the ORR i-t curves of Pt/C and Co@Ru/CS at +0.70 V in an O_2-saturated 0.1 M KOH solution at an electrode rotation rate of 900 rpm. After 20 h's continuous operation, the ORR current of Co@Ru/CS diminished by only 10 % while Pt/C showed a loss of 42 %. Similar results were obtained in ADT (Fig. S9b). After 5000 CV cycles (within +1.0 to +0.6 V), the $E_{1/2,\ ORR}$ of Co@Ru/CS shifted negatively by only 14 mV, much smaller than that of Pt/C (40 mV). Notably, after OER i-t tests at +1.45 V, a negative shift of only 36 mV was observed with the $E_{1/2,\ ORR}$ of Co@Ru/CS (Fig. S9c), likely because of the robust structures of the N dopants and CoN_x moieties.

For OER (Fig. 3**i**), after 1000 CV cycles (+1.20 to +1.60 V), the OER LSV curve showed a positive potential shift of merely 15 mV at the current density of 10 mA cm^{-2}, as compared to 50 mV for RuO_2. In addition, after continuous i-*t* test for 36 h (at +1.5 V), ca. 60.0 % of the current density was lost with commercial RuO_2, whereas only ca. 30 % for Co@Ru/CS. These results demonstrate that Co@Ru/CS possessed better stability towards ORR and OER than commercial Pt/C and RuO_2 in alkaline media.

3.3. *Electrocatalytic enhancement mechanism*

It is worth noting that the electrocatalysts often undergo significant restructuring at high potentials during oxygen electrochemistry [43]. Thus, to accurately reveal the active and stability, the structure and chemical composition of Co@Ru/CS after i-t tests for ORR and OER were studied by XRD, TEM, XPS and Raman measurements. From the XRD patterns in Fig. S10a, the diffraction peaks of Co can still be found after ORR tests, and in HRTEM measurements (Fig. S10b), RuO_2 (lattice spacing 0.318 nm) and Co (lattice spacing 0.20 nm) can both be readily identified, suggesting oxidization of Ru. After OER tests, the XRD patterns of CoOOH and RuO_2 started to emerge (Fig. S11a), indicating apparent reconfiguration of Co@Ru/CS. HRTEM measurements (Fig. S11b–d) further confirm the results, where the lattice fringes of

CoOOH and RuO_2 can be readily resolved. In Raman measurements (Fig. S12), the I_D/I_G value can be found to increase only slightly to 1.21 and 1.14 after OER and ORR tests, respectively, suggesting a largely intact carbon scaffold during the electrochemical reactions. Yet, ICP-MS measurements showed that ca. 10 % of the initial Ru was dissolved from Co@Ru@CS into the electrolyte during OER, whereas the dissolution was significantly reduced (<1%) during ORR (Table S2). In fact, the S number, which is the mole ratio of O_2 produced versus dissolved Ru ($n_{O2,evolved}/n_{Ru,dissolved}$) [44,45], can be found to be rather consistent at 5.4×10^4, 5.4×10^4 and 5.1×10^4 at 4, 8, and 12 h of OER, respectively (Fig. S13 and Table S3), further confirming the excellent OER performance of Co@Ru/CS.

Moreover, XPS measurements of the C 1s and N 1s electrons after OER and ORR tests (Fig. S14a and b) also suggest that the carbon matrix possessed good stability, retaining the C=C, Co–N, pyridinic-N and graphitic-N species. In the Ru 3p spectra (Fig. S14c), the Ru^0 species disappeared completely after OER and ORR tests. In the Co 2p spectra (Fig. S14d) after ORR test, the Co^0 peak can be still observed, but shifted to a higher energy after OER, suggesting marked oxidation of the Co@Ru/CS surface. This is consistent with the formation of RuO_2 and CoOOH observed above. In addition, in situ Raman measurements were carried out to examine the surface structure of Co@Ru/CS during OER tests (the experimental setup is depicted in Fig. 4**a**). Fig. 4**b** shows the Raman spectra of Co@Ru/CS acquired at different applied potentials. No obvious peak appeared when the potential was under +1.3 V. Yet, at increasingly positive potentials, three vibrational bands emerged, which can be assigned to RuO_2 (684 cm^{-1}) and CoOOH (476 and 517 cm^{-1}), respectively [44,45], in alignment with the results from the above XPS, XRD, and HRTEM analyses. That is, the excellent OER activity of Co@Ru/CS most likely arose from the RuO_2/CoOOH species generated during electrochemical reactions [46].

DFT calculations were then carried out to further analyze the OER mechanism. The OER process on the surface of CoOOH/RuO_2 is a typical 4-electron transfer reaction involving multiple oxygen-containing

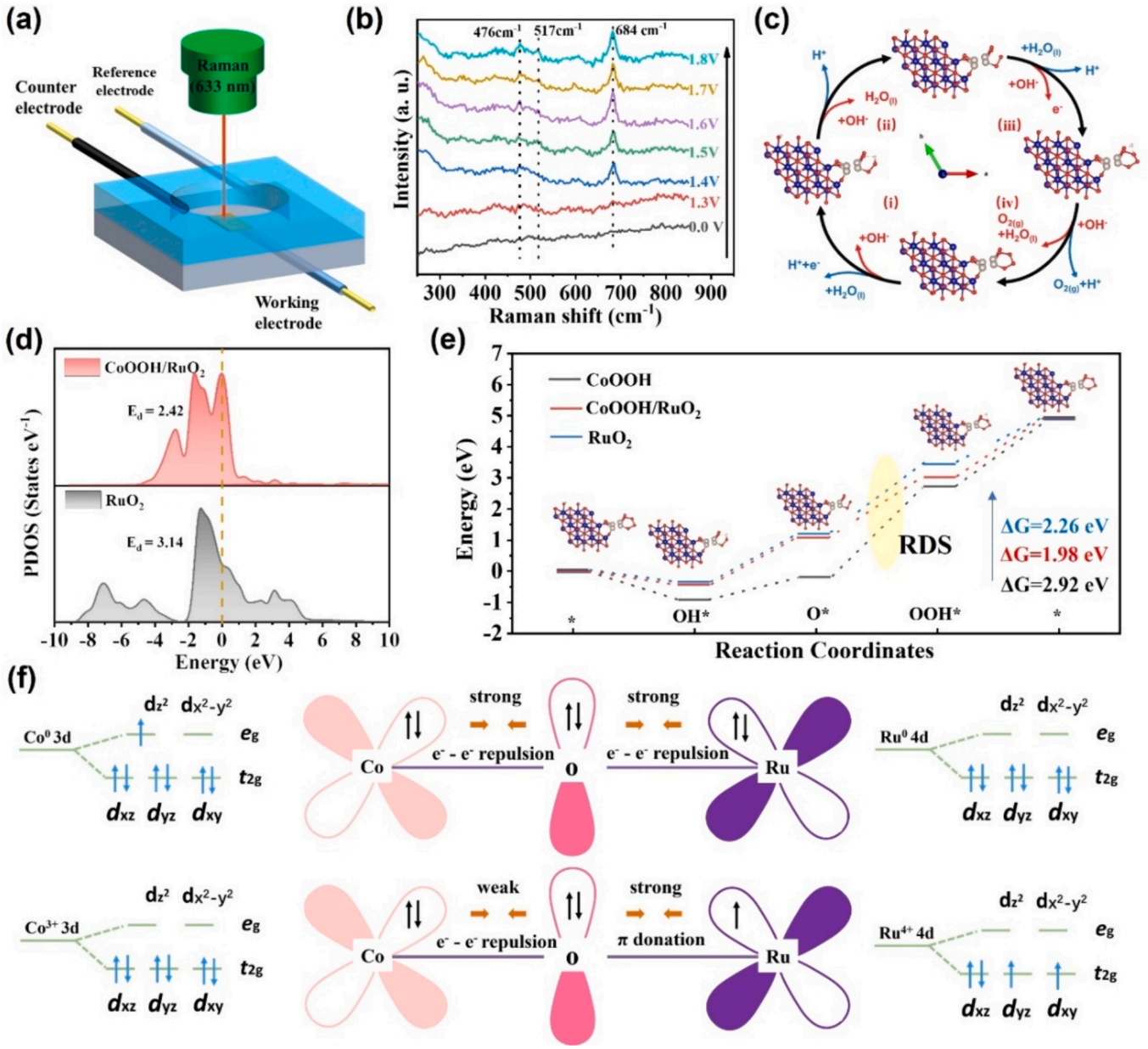

Fig. 4. (a) Schematic diagram of the in situ Raman test set-up. (b) In situ Raman spectra of Co@Ru/CS at different applied potentials for OER. (c) Structural model for OER on the surface of CoOOH/RuO_2. (d) PDOS plots of CoOOH/RuO_2 and CoOOH. (e) ΔG of CoOOH/RuO_2 and RuO_2 in different steps of OER. (f) Schematic diagram of Ru-Co electronic configuration-dependent orbital interactions.

intermediates, such as *OH, *O, *OOH, and O_2 [47], and the main adsorption sites for oxygen-containing intermediates in the CoOOH/RuO_2 heterojunction are the Ru centers (Fig. 4**c**). Fig. 4**d** shows the density of states (DOS), where the d-band center (−2.42 eV) of Ru in CoOOH/RuO_2 is close to the Fermi level, as compared to pristine RuO_2 (−3.14 eV), which can boost the binding of reaction intermediates and hence charge transfer during the OER process, leading to an improved electrocatalytic performance [48]. For OER catalysts, the performance depends mainly on the Gibbs free energy change of the rate-determining step (RDS) [49]. As shown in Fig. 4**e**, the RDS is the coupling of O* to OOH*, where Co@Ru/CS displays a lowest ΔG of only 1.98 eV, as compared to 2.26 eV for RuO_2 and 2.92 eV for CoOOH, in agreement with experimental results.

Further mechanistic insights were obtained by analysis of the materials electronic configurations using molecular orbital theory. Considering the electronic configurations of Co^0 ($3d^7$: $t_{2g}^6e_g^1$) and Ru^0 ($4d^6$: $t_{2g}^6e_g^0$) in the Ru-Co NPs (Fig. 4**f**), the fully occupied π-symmetry (t_{2g}) 3d orbitals of Co^0 and 4d orbitals of Ru^0 in low spin state interact with bridging O^{2-} through strong e^--e^- repulsion. After reconstruction, there are two unpaired electrons in the π-symmetry (t_{2g}) 4d orbitals of Ru^{4+} ($4d^4$: $t_{2g}^4e_g^0$) which interact with the bridging O^{2-} through π donation and weaken the e^--e^- repulsion between the bridging O^{2-} and Co^{3+} ($3d^6$: $t_{2g}^6e_g^0$), trigger partial electron transfer from Co^{3+} to Ru^{4+} and thus promote electron transfer at the interface [50,51].

The partial density of state (PDOS) is shown in Fig. 5**a**, which confirms the changes in the spin configuration after reconstruction. One can see that the total occupancy of the t_{2g} orbitals is very close at 3.93 for Co@Ru/CS and 3.94 for RuO_2. Yet, the total occupancy of the e_g orbitals is only 2.0 for Ru in Co@Ru/CS and 1.8 for RuO_2. The decrease of the e_g orbital occupancy after reconstruction can be ascribed to the interactions between the Co 3*d*, O 2*p* and Ru 4*d* electrons, due to reduced spin of Ru after transformation into RuO_2.

During the OER process, the reaction intermediates (*OH, *O, *OOH and *OO) would adsorb on the active sites and finally evolve into O_2 (Fig. 5**b**). During the adsorption process, due to symmetry conservation, the Ru $d_{x^2-y^2}$ and d_{xy} orbitals are not considered. The Ru d_{z^2} orbitals are axial-symmetric with O p_z orbitals and would form σ/σ* molecular orbitals while the Ru d_{xz} and d_{yz} are mirror-symmetric with O p_x/p_y and would form π/π* molecular orbitals [52]. Meanwhile, the bond orders (BO) are used to evaluate the adsorption of the reaction intermediates by the following equation, BO = ($n_{bonding}$ - $n_{anti\text{-}bonding}$)/2, where $n_{bonding}$ and $n_{anti\text{-}bonding}$ represent the number of electrons in the bonding and anti-bonding states, respectively. The higher the BO, the stronger the adsorption. Fig. 5**c** shows the spin configurations of Ru^{4+}. For high-spin Ru^{4+} species, the adsorption of all oxygen intermediates is too strong (Fig. 5**d**). Low-spin Ru^{4+} entails a strong adsorption of *OH (Fig. 5**e**), with a BO of 2, which is beneficial to capture the reactant and start the OER cycle, whereas medium adsorption is observed with *O, *OOH and *OO intermediates, which is conducive to the transformation of reaction intermediates during the OER process. This suggests that the spin configurations of cations determine their interactions with reaction intermediates, rendering the lower-spin Ru^{4+} more favorable for the OER process.

3.4. Performance of r-ZABs

Results from the above studies show that Co@Ru/CS can serve as an effective bifunctional oxygen electrocatalyst (Fig. 6**a**), where the pyridinic-N, graphitic-N, and Co-N contributed collectively to the ORR activity, and the CoOOH/RuO_2 heterojunctions derived from surface reconstruction were responsible for OER. In electrochemical measurements (Fig. 6**b**), Co@Ru/CS exhibited a small ΔE of only 0.69 V, markedly lower than that of commercial benchmarks of Pt/C + RuO_2 (0.76 V). In fact, the bifunctional activity of Co@Ru/CS was even competitive to leading results of relevant catalysts reported in the literature (Fig. S15) [10,13,15–17,53–57].

The excellent overall oxygen catalytic performance made Co@Ru/CS a viable air cathode catalyst for r-ZABs. In Fig. 6**c, a** r-ZAB was fabricated by using a Zn foil as the anode and a piece of carbon cloth coated with Co@Ru/CS as the air electrode, along with 6.0 M KOH + 0.2 M Zn $(Ac)_2$ as the electrolyte (Fig. S16a). First, the specific capacity was tested at a discharge current density of 10.0 mA cm^{-2} (Fig. 6**d**), which was 781 mAh g_{Zn}^{-1} for Co@Ru/CS, higher than that for Pt/C + RuO_2 (760.56 mAh g_{Zn}^{-1}). Moreover, from Fig. 6**e**, one can find that the discharge–charge overpotential of Co@Ru/CS was slightly lower than that of Pt/C + RuO_2, where Co@Ru/CS-based r-ZAB delivered a low voltage difference of 0.99 V at 50.0 mA cm^{-2}, as compared to 1.06 V for Pt/C + RuO_2. In the discharge mode (Fig. 6**f**), the Co@Ru/CS-based r-ZAB exhibited a current density of 109.2 mA cm^{-2} at 1.0 V and a maximum power density of 115 mW cm^{-2} at 0.83 V, while the maximum power density of the Pt/C

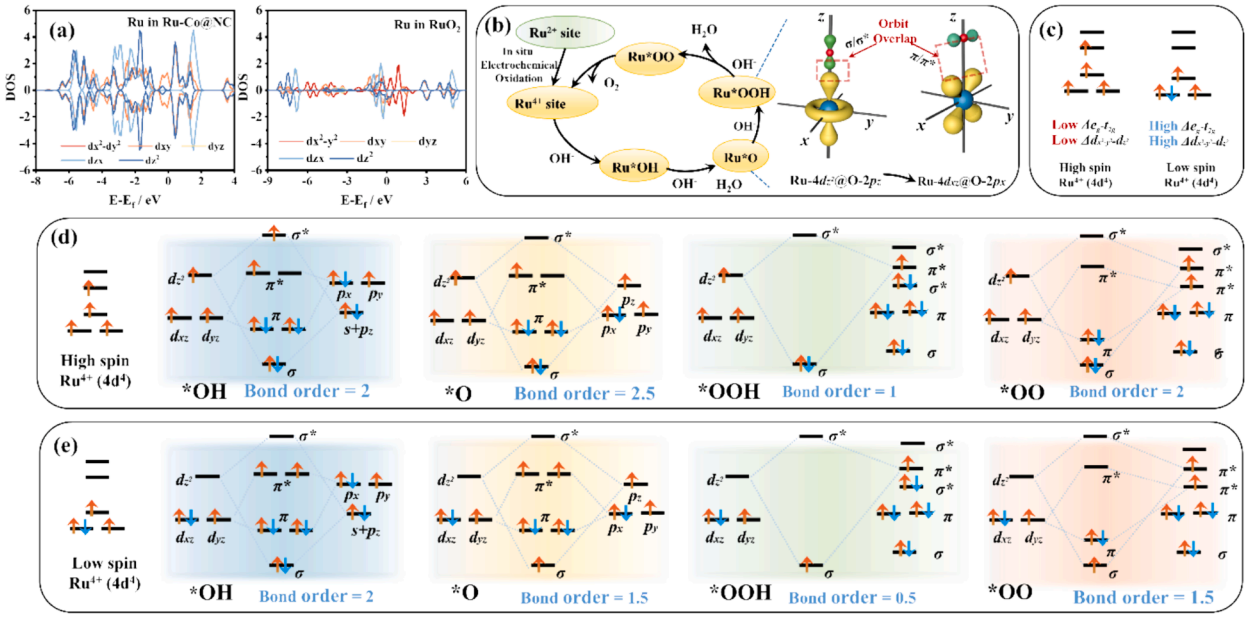

Fig. 5. (a) PDOS plots of Co@Ru/CS and RuO_2. (b) Spin configurations of Ru^{4+}. (c) Reaction intermediates of *OH, *O, *OOH and *OO adsorbed on the Ru sites. Coupling with oxygen-related intermediates for (d) high-spin state of Ru^{4+} species and (e) low-spin state of Ru^{4+}.

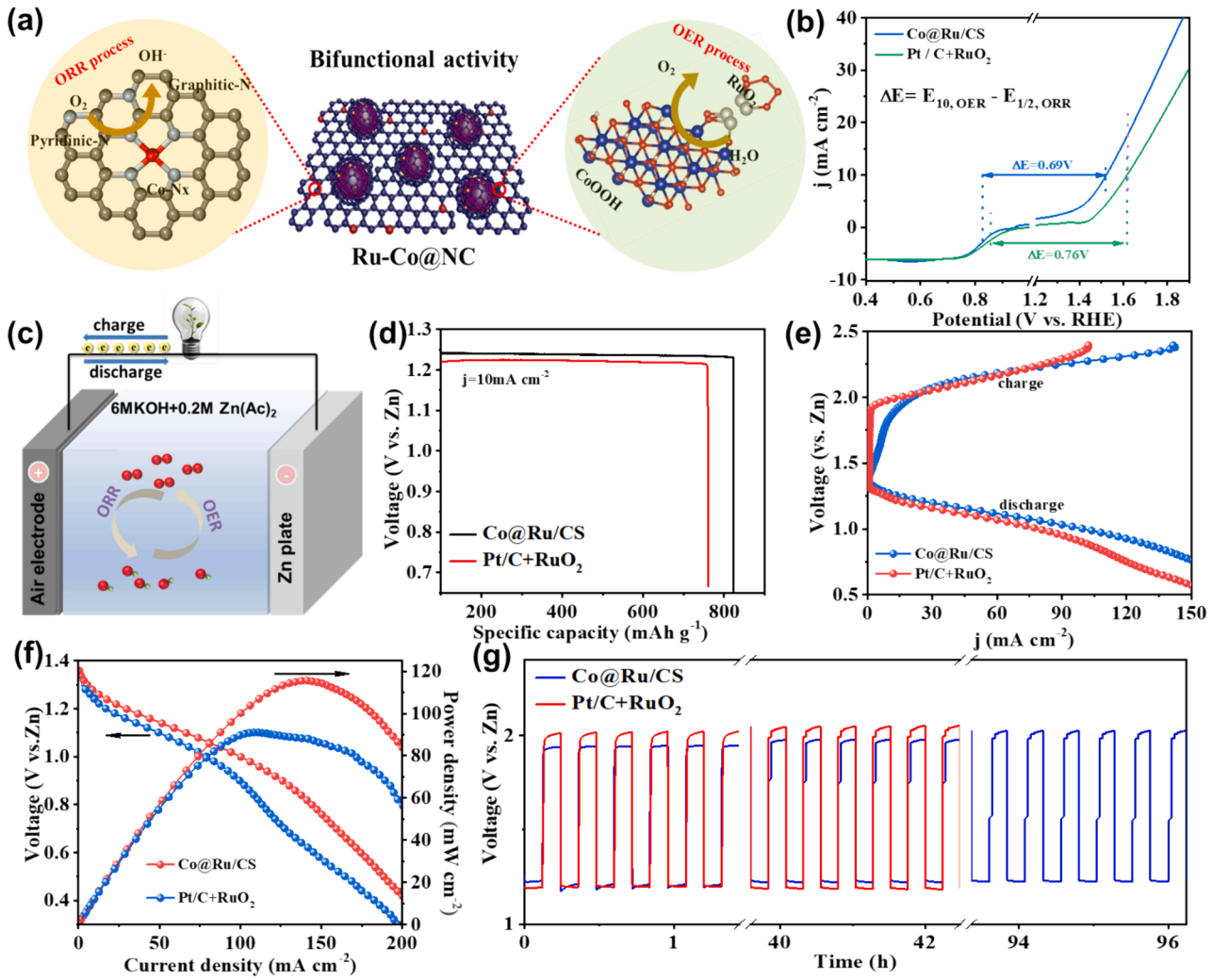

Fig. 6. (a) Structural models of OER/ORR active sites in Co@Ru/CS. (b) Overall LSVs of OER and ORR of Co@Ru/CS and Pt/C + RuO_2. (c) Schematic of a home-made r-ZAB. (d) Specifc capacities of r-RABs based on Pt + RuO_2 and Co@Ru/CS. (e) Discharging and charging polarization curves and (f) discharge polarization (V–j) curves and the corresponding power density curves of r-ZABs based on Pt + RuO_2 and Co@Ru/CS. (g) Long-term charging and discharge curves at 10 mA cm^{-2} of the primary r-ZABs for Co@Ru/CS and Pt/C + RuO_2.

+ RuO_2 based device was markedly lower at 91 mW cm^{-2}, further confirming the excellent reversible oxygen catalytic activity of Co@Ru/CS.

Co@Ru/CS-based r-ZAB also displayed a higher open circuit voltage of 1.447 V, as compared to 1.412 V for Pt/C + RuO_2 (Fig. S16b). Notably, a light-emitting diode could be powered by two r-ZABs and run for several hours (Fig. S16b inset). These indicate excellent performance of the Co@Ru/CS-based r-ZAB. Fig. 6**g** shows the long-term cycling curves at 10 mA cm^{-2} of the r-ZAB, where the charge–discharge voltage difference of Co@Ru/CS and Pt/C + RuO_2 remained at 0.72 V and 0.80 V, respectively. During continuous operation for 40 h, it increased to 0.86 V with the Pt/C + RuO_2-based r-ZAB, but remained at 0.76 V for the Co@Ru/CS-based counterpart. More importantly, after 96 h's continuous operation, the Co@Ru/CS-based r-ZAB remained stable. These results highlight the remarkable performance of Co@Ru/CS as the oxygen catalysts for r-ZAB.

4. Conclusion

In summary, nanocomposites based on Co@Ru core@shell nanoparticles embedded within N-doped carbon (Co@Ru/CS) were prepared via facile galvanic exchange reactions between $RuCl_3$ and Co/CS and exhibited apparent bifunctional electrocatalytic activity towards both OER and ORR. Electrochemical tests showed that the Co@Ru/CS composite exhibited a low $\eta_{10,OER}$ of +180 mV and a high $E_{1/2,ORR}$ of +0.832 V, an excellent activity remarkably outperforming the monometallic Ru/NC and Co/CS counterparts. In conjunction with computational studies, the OER activity of Co@Ru/CS was found to be mainly due to RuO_2/CoOOH species produced at high electrode potentials of OER, whereas ORR was most likely due to the N-doped carbon and CoN_x moieties. With Co@Ru/CS as the air cathode catalyst, the r-ZAB displayed a higher specific capacity (781 mAh g_{Zn}^{-1}), larger power density (115 mW cm^{-2}) and better long-term cycling stability than that based on commercial Pt/C + RuO_2. These results offer a unique strategy of structural engineering, contributing to the design of efficient bifunctional catalysts for r-ZABs.

CRediT authorship contribution statement

Shunlian Ning: Writing – original draft, Formal analysis, Data curation. **Jiayu Lao:** Formal analysis, Data curation. **Wei Zhou:** Data curation. **Yanting Ye:** Formal analysis. **Qikai Wu:** Formal analysis. **Mingzhe Chen:** Formal analysis. **Ming-Hsien Lee:** Formal analysis. **Tianchen Cui:** Writing – original draft, Formal analysis. **Dengke Zhao:** Writing – original draft, Methodology, Formal analysis, Conceptualization. **Nan Wang:** Writing – original draft, Methodology, Funding

acquisition, Data curation, Conceptualization. **Shaowei Chen:** Writing – review & editing, Resources, Methodology, Conceptualization.

Declaration of competing interest

The authors declare that they have no known competing financial interests or personal relationships that could have appeared to influence the work reported in this paper.

Data availability

Data will be made available on request.

Acknowledgements

This work was supported by the National Natural Science Foundation of China (22209056); the Postdoctoral Research Foundation of China (2020M673071); the Special Funds for the Cultivation of Guangdong College Students' Scientific and Technological Innovation (pdjh2022b0065); the Guangdong Basic and Applied Basic Research Foundation (2023A1515010270); the Science and Technology Planning Project of Guangzhou (201605030008, 202201010125) and the National Innovation and Entrepreneurship Training Program for Undergraduate (202110559044). S. W. C. acknowledges partial support from the National Science Foundation (CHE-1900235).

Appendix A. Supplementary data

Supplementary data to this article can be found online at https://doi.org/10.1016/j.jcat.2024.115532.

References

[1] X. Zhu, C. Hu, R. Amal, L. Dai, X. Lu, Heteroatom-doped carbon catalysts for zinc–air batteries: progress, mechanism, and opportunities, Energy Environ. Sci. 13 (2020) 4536–4563.
[2] C.-X. Zhao, J.-N. Liu, J. Wang, D. Ren, B.-Q. Li, Q. Zhang, Recent advances of noble-metal-free bifunctional oxygen reduction and evolution electrocatalysts, Chem. Soc. Rev. 50 (2021) 7745–7778.
[3] W. Niu, S. Pakhira, K. Marcus, Z. Li, J.L. Mendoza-Cortes, Y. Yang, Apically dominant mechanism for improving catalytic activities of N-doped carbon nanotube arrays in rechargeable zinc-air battery, Adv. Energy Mater. 8 (2018) 1800480.
[4] H.-F. Wang, L. Chen, H. Pang, S. Kaskel, Q. Xu, MOF-derived electrocatalysts for oxygen reduction, oxygen evolution and hydrogen evolution reactions, Chem. Soc. Rev. 49 (2020) 1414–1448.
[5] J. Pan, Y.Y. Xu, H. Yang, Z. Dong, H. Liu, B.Y. Xia, Advanced architectures and relatives of air electrodes in Zn–Air batteries, Adv. Sci. 5 (2018) 1700691.
[6] Y.-R. Hao, H. Xue, L. Lv, J. Sun, N. Guo, T. Song, H. Dong, J. Zhang, Q. Wang, Unraveling the synergistic effect of defects and interfacial electronic structure modulation of pealike CoFe@Fe3N to achieve superior oxygen reduction performance, Appl. Catal. b: Environ. 295 (2021) 120314.
[7] J. Ban, X. Wen, H. Xu, Z. Wang, X. Liu, G. Cao, G. Shao, J. Hu, Dual evolution in defect and morphology of single-atom dispersed carbon based oxygen electrocatalyst, Adv. Funct. Mater. 31 (2021) 2010472.
[8] Y. Guo, Y.-N. Chen, H. Cui, Z. Zhou, Bifunctional electrocatalysts for rechargeable Zn-air batteries, Chin. J. Catal. 40 (2019) 1298–1310.
[9] W. Niu, A. Jeyaranjan, S. Seal, Y. Yang, Correction to amorphous MOF introduced N-doped graphene: an efficient and versatile electrocatalyst for zinc-air battery and water splitting, ACS Appl. Energy Mater. 1 (2018) 4413.
[10] Z. Chen, X. Peng, Z. Chen, T. Li, R. Zou, G. Shi, Y. Huang, P. Cui, J. Yu, Y. Chen, X. Chi, K.P. Loh, Z. Liu, X. Li, L. Zhong, J. Lu, Mass production of sulfur-tuned single-atom catalysts for Zn–Air batteries, Adv. Mater. 35 (2023) 2209948.
[11] K. Wu, L. Zhang, Y. Yuan, L. Zhong, Z. Chen, X. Chi, H. Lu, Z. Chen, R. Zou, T. Li, C. Jiang, Y. Chen, X. Peng, J. Lu, An iron-decorated carbon aerogel for rechargeable flow and flexible Zn–Air batteries, Adv. Mater. 32 (2020) 2002292.
[12] Y. Wang, H. Su, Y. He, L. Li, S. Zhu, H. Shen, P. Xie, X. Fu, G. Zhou, C. Feng, D. Zhao, F. Xiao, X. Zhu, Y. Zeng, M. Shao, S. Chen, G. Wu, J. Zeng, C. Wang, Advanced electrocatalysts with single-metal-atom active sites, Chem. Rev. 120 (2020) 12217–12314.
[13] K.R. Yoon, C.-K. Hwang, S.-H. Kim, J.-W. Jung, J.E. Chae, J. Kim, K.A. Lee, A. Lim, S.-H. Cho, J.P. Singh, J.M. Kim, K. Shin, B.M. Moon, H.S. Park, H.-J. Kim, K. H. Chae, H.C. Ham, I.-D. Kim, J.Y. Kim, Hierarchically assembled cobalt oxynitride nanorods and n-doped carbon nanofibers for efficient bifunctional oxygen electrocatalysis with exceptional regenerative efficiency, ACS Nano 15 (2021) 11218–11230.
[14] H. Yang, S. Gao, D. Rao, X. Yan, Designing superior bifunctional electrocatalyst with high-purity pyrrole-type CoN4 and adjacent metallic cobalt sites for rechargeable Zn-air batteries, Energy Storage Mater. 46 (2022) 553–562.
[15] K. Ding, J. Hu, J. Luo, L. Zhao, W. Jin, Y. Liu, Z. Wu, G. Zou, H. Hou, X. Ji, Robust electronic correlation of Co-CoN4 hybrid active sites for durable rechargeable Zn-Air batteries, Adv. Funct. Mater. 32 (2022) 2207331.
[16] Q. Xu, L. Peng, K. Luo, J. Zhong, C. Zhang, D. Yuan, CoSe2 nanoparticles anchored on CoNC carbon nanoplates as bifunctional electrocatalyst for flexible rechargeable Zn-air batteries, J. Colloid Interface Sci. 643 (2023) 73–81.
[17] Q. Wang, Y. Lei, Z. Chen, N. Wu, Y. Wang, B. Wang, Y. Wang, Fe/Fe_3C@C nanoparticles encapsulated in N-doped graphene–CNTs framework as an efficient bifunctional oxygen electrocatalyst for robust rechargeable Zn–air batteries, J. Mater. Chem. A 6 (2018) 516–526.
[18] N. Wang, S. Ning, X. Yu, D. Chen, Z. Li, J. Xu, H. Meng, D. Zhao, L. Li, Q. Liu, B. Lu, S. Chen, Graphene composites with Ru-RuO2 heterostructures: Highly efficient Mott–Schottky-type electrocatalysts for pH-universal water splitting and flexible zinc–air batteries, Appl. Catal. b: Environ. 302 (2022) 120838.
[19] Y. Li, W. Wang, M. Cheng, Y. Feng, X. Han, Q. Qian, Y. Zhu, G. Zhang, Arming Ru with oxygen-vacancy-enriched RuO2 sub-nanometer skin activates superior bifunctionality for pH-universal overall water splitting, Adv. Mater. 35 (2023) 2206351.
[20] D. Zhao, J. Dai, N. Zhou, N. Wang, P. Xinwen, Y. Qu, L. Li, Prussian blue analogues-derived carbon composite with cobalt nanoparticles as an efficient bifunctional electrocatalyst for oxygen reduction and hydrogen evolution, Carbon 142 (2019) 196–205.
[21] R. Wang, K. Lu, J. Zhang, X. Li, Z. Zheng, Regulation of the Co–Nx active sites of MOF-templated Co@NC catalysts via au doping for boosting oxidative esterification of alcohols, ACS Catal. 12 (2022) 14290–14303.
[22] C. Shi, Y. Liu, R. Qi, J. Li, J. Zhu, R. Yu, S. Li, X. Hong, J. Wu, S. Xi, L. Zhou, L. Mai, Hierarchical N-doped carbon spheres anchored with cobalt nanocrystals and single atoms for oxygen reduction reaction, Nano Energy 87 (2021) 106153.
[23] X. Kang, F. Yang, Z. Zhang, H. Liu, S. Ge, S. Hu, S. Li, Y. Luo, Q. Yu, Z. Liu, Q. Wang, W. Ren, C. Sun, H.-M. Cheng, B. Liu, A corrosion-resistant RuMoNi catalyst for efficient and long-lasting seawater oxidation and anion exchange membrane electrolyzer, Nat. Commun. 14 (2023) 3607.
[24] D. Eisenberg, W. Stroek, N.J. Geels, C.S. Sandu, A. Heller, N. Yan, G. Rothenberg, A simple synthesis of an N-doped carbon ORR catalyst: hierarchical micro/meso/macro porosity and graphitic shells, Chem-Eur. J. 22 (2016) 501–505.
[25] W. Niu, L. Li, X. Liu, N. Wang, J. Liu, W. Zhou, Z. Tang, S. Chen, Mesoporous N-doped carbons prepared with thermally removable nanoparticle templates: an efficient electrocatalyst for oxygen reduction reaction, J. Am. Chem. Soc. 137 (2015) 5555–5562.
[26] S. Chen, T. Luo, X. Li, K. Chen, J. Fu, K. Liu, C. Cai, Q. Wang, H. Li, Y. Chen, C. Ma, L. Zhu, Y.-R. Lu, T.-S. Chan, M. Zhu, E. Cortés, M. Liu, Identification of the highly active Co–N4 coordination motif for selective oxygen reduction to hydrogen peroxide, J. Am. Chem. Soc. 144 (2022) 14505–14516.
[27] M. Lao, G. Zhao, P. Li, T. Ma, Y. Jiang, H. Pan, S.X. Dou, W. Sun, Manipulating the coordination chemistry of Ru–N(O)–C moieties for fast alkaline hydrogen evolution kinetics, Adv. Funct. Mater. 31 (2021) 2100698.
[28] Y. Li, Y. Luo, Z. Zhang, Q. Yu, C. Li, Q. Zhang, Z. Zheng, H. Liu, B. Liu, S. Dou, Implanting Ru nanoclusters into N-doped graphene for efficient alkaline hydrogen evolution, Carbon 183 (2021) 362–367.
[29] H. Yan, Z. Jiang, B. Deng, Y. Wang, Z.-J. Jiang, Ultrathin carbon coating and defect engineering promote RuO2 as an efficient catalyst for acidic oxygen evolution reaction with super-high durability, Adv. Energy Mater. 13 (2023) 2300152.
[30] Y. Zhong, Y. Lu, Z. Pan, J. Yang, G. Du, J. Chen, Q. Zhang, H. Zhou, J. Wang, C. Wang, W. Li, Efficient water splitting system enabled by multifunctional platinum-free electrocatalysts, Adv. Funct. Mater. 31 (2021) 2009853.
[31] M.-R. Liu, Q.-L. Hong, Q.-H. Li, Y. Du, H.-X. Zhang, S. Chen, T. Zhou, J. Zhang, Cobalt boron imidazolate framework derived cobalt nanoparticles encapsulated in B/N codoped nanocarbon as efficient bifunctional electrocatalysts for overall water splitting, Adv. Funct. Mater. 28 (2018) 1801136.
[32] A.M. Harzandi, S. Shadman, A.S. Nissimagoudar, D.Y. Kim, H.-D. Lim, J.H. Lee, M. G. Kim, H.Y. Jeong, Y. Kim, K.S. Kim, Ruthenium core-shell engineering with nickel single atoms for selective oxygen evolution via nondestructive mechanism, Adv. Energy Mater. 11 (2021) 2003448.
[33] T. He, Y. Peng, Q. Li, J.E. Lu, Q. Liu, R. Mercado, Y. Chen, F. Nichols, Y. Zhang, S. Chen, Nanocomposites based on ruthenium nanoparticles supported on cobalt and nitrogen-codoped graphene nanosheets as bifunctional catalysts for electrochemical water splitting, ACS Appl. Mater. Interfaces 11 (2019) 46912–46919.
[34] W. Wang, S. Xi, Y. Shao, W. Sun, S. Wang, J. Gao, C. Mao, X. Guo, G. Li, Oxide passivated CoNi@NC-supported Ru(OH)xCly cluster as highly efficient catalysts for the oxygen and hydrogen evolution, ACS Sustain. Chem. Eng. 7 (2019) 17227–17236.
[35] C. Wang, L. Qi, Heterostructured inter-doped ruthenium-cobalt oxide hollow nanosheet arrays for highly efficient overall water splitting, Angew. Chem. Int. Ed. 59 (2020) 17219–17224.
[36] M. Yang, T. Feng, Y. Chen, J. Liu, X. Zhao, B. Yang, Synchronously integration of Co, Fe dual-metal doping in Ru@C and CDs for boosted water splitting performances in alkaline media, Appl. Catal. b: Environ. 267 (2020) 118657.
[37] K. Shah, R. Dai, M. Mateen, Z. Hassan, Z. Zhuang, C. Liu, M. Israr, W.-C. Cheong, B. Hu, R. Tu, C. Zhang, X. Chen, Q. Peng, C. Chen, Y. Li, Cobalt single atom incorporated in ruthenium oxide sphere: a robust bifunctional electrocatalyst for HER and OER, Angew. Chem. Int. Ed. 61 (2022) e202114951.

[38] J. Liu, Y. Zheng, Y. Jiao, Z. Wang, Z. Lu, A. Vasileff, S. Qiao, NiO as a bifunctional promoter for RuO2 toward superior overall water splitting, Small 14 (2018) 1704073.
[39] Q. Qin, H. Jang, L. Chen, G. Nam, X. Liu, J. Cho, Low loading of RhxP and RuP on N, P codoped carbon as two trifunctional electrocatalysts for the oxygen and hydrogen electrode reactions, Adv. Energy Mater. 8 (2018) 1801478.
[40] D. Liu, H. Xu, C. Wang, C. Ye, R. Yu, Y. Du, In situ etch engineering of Ru doped NiFe(OH)x/NiFe-MOF nanocomposites for boosting the oxygen evolution reaction, J. Mater. Chem. A 9 (2021) 24670–24676.
[41] C.-B. Hong, X. Li, W.-B. Wei, X.-T. Wu, Q.-L. Zhu, Nano-engineering of Ru-based hierarchical porous nanoreactors for highly efficient pH-universal overall water splitting, Appl. Catal. b: Environ. 294 (2021) 120230.
[42] I.S. Kwon, T.T. Debela, I.H. Kwak, Y.C. Park, J. Seo, J.Y. Shim, S.J. Yoo, J.-G. Kim, J. Park, H.S. Kang, Ruthenium nanoparticles on cobalt-doped 1T′ phase MoS2 nanosheets for overall water splitting, Small 16 (2020) 2000081.
[43] X. Liu, K. Ni, B. Wen, R. Guo, C. Niu, J. Meng, Q. Li, P. Wu, Y. Zhu, X. Wu, L. Mai, Deep reconstruction of nickel-based precatalysts for water oxidation catalysis, ACS Energy Lett. 4 (2019) 2585–2592.
[44] M.A. Hubert, A.M. Patel, A. Gallo, Y. Liu, E. Valle, M. Ben-Naim, J. Sanchez, D. Sokaras, R. Sinclair, J.K. Nørskov, L.A. King, M. Bajdich, T.F. Jaramillo, Acidic oxygen evolution reaction activity-stability relationships in Ru-based pyrochlores, ACS Catal. 10 (2020) 12182–12196.
[45] J. Edgington, L.C. Seitz, Advancing the rigor and reproducibility of electrocatalyst stability benchmarking and intrinsic material degradation analysis for water oxidation, ACS Catal. 13 (2023) 3379–3394.
[46] Q. Liu, S. McNair, F. Nichols, B. Lu, B. Yu, D. Pan, J. Ko, A. Bhuller, F. Bridges, S. Chen, Ultrafast synthesis of cobalt/carbon nanocomposites by magnetic induction heating for oxygen evolution reaction, Adv. Sens. Energy Mater. 2 (2023) 100046.
[47] N.-T. Suen, S.-F. Hung, Q. Quan, N. Zhang, Y.-J. Xu, H.M. Chen, Electrocatalysis for the oxygen evolution reaction: recent development and future perspectives, Chem. Soc. Rev. 46 (2017) 337–365.
[48] Y. Gu, A. Wu, Y. Jiao, H. Zheng, X. Wang, Y. Xie, L. Wang, C. Tian, H. Fu, Two-dimensional porous molybdenum phosphide/nitride heterojunction nanosheets for pH-universal hydrogen evolution reaction, Angew. Chem. Int. Ed. 60 (2021) 6673–6681.
[49] J. Dai, D. Zhao, W. Sun, X. Zhu, S. Chen, Cu(II) ions induced structural transformation of cobalt selenides for remarkable enhancement in oxygen/hydrogen electrocatalysis, ACS Catal. 2019 (2019).
[50] X. Li, M. Chen, Y. Ye, C. Chen, Z. Li, Y. Zhou, J. Chen, F. Xie, Y. Jin, N. Wang, H. Meng, Electronic structure modulation of nickel sites by cationic heterostructures to optimize ethanol electrooxidation activity in alkaline solution, Small 19 (2023) 2207086.
[51] Q. Qian, X. He, Z. Li, Y. Chen, Y. Feng, M. Cheng, H. Zhang, W. Wang, C. Xiao, G. Zhang, Y. Xie, Electrochemical biomass upgrading coupled with hydrogen production under industrial-level current density, Adv. Mater. 35 (2023) 2300935.
[52] J.O.M. Bockris, T. Otagawa, The electrocatalysis of oxygen evolution on perovskites, J. Electrochem. Soc. 131 (1984) 290.
[53] R.S. Kumar, S. Prabhakaran, S. Ramakrishnan, S.C. Karthikeyan, A.R. Kim, D. H. Kim, D.J. Yoo, Developing outstanding bifunctional electrocatalysts for rechargeable Zn-air batteries using high-purity spinel-type $ZnCo_2Se_4$ nanoparticles, Small 19 (2023) 2207096.
[54] P. Du, K. Hu, J. Lyu, H. Li, X. Lin, G. Xie, X. Liu, Y. Ito, H.-J. Qiu, Anchoring Mo single atoms/clusters and N on edge-rich nanoporous holey graphene as bifunctional air electrode in Zn-air batteries, Appl. Catal. b: Environ. 276 (2020) 119172.
[55] H. Zhang, M. Zhao, H. Liu, S. Shi, Z. Wang, B. Zhang, L. Song, J. Shang, Y. Yang, C. Ma, L. Zheng, Y. Han, W. Huang, Ultrastable FeCo bifunctional electrocatalyst on Se-doped CNTs for liquid and flexible all-solid-state rechargeable Zn–Air batteries, Nano Lett. 21 (2021) 2255–2264.
[56] C. Jiao, Z. Xu, J. Shao, Y. Xia, J. Tseng, G. Ren, N. Zhang, P. Liu, C. Liu, G. Li, S. Chen, S. Chen, H.-L. Wang, High-density atomic Fe–N4/C in tubular, biomass-derived, nitrogen-rich porous carbon as air-electrodes for flexible Zn–Air batteries, Adv. Funct. Mater. 33 (2023) 2213897.
[57] D. Ji, L. Fan, L. Li, S. Peng, D. Yu, J. Song, S. Ramakrishna, S. Guo, Atomically transition metals on self-supported porous carbon flake arrays as binder-free air cathode for wearable zinc-air batteries, Adv. Mater. 31 (2019) 1808267.